JGR Space Physics

RESEARCH ARTICLE
10.1029/2022JA031036

# Lower Hybrid Waves in High Altitude Echoes of the Topside Equatorial Ionosphere

**S. Derghazarian[1], E. L. Rojas[1], D. L. Hysell[1], and C. E. Seyler[2]**

[1]Earth and Atmospheric Sciences, Cornell University, Ithaca, NY, USA, [2]School of Electrical and Computer Engineering, Cornell University, Ithaca, NY, USA

**Key Points:**

- Lower hybrid lines were observed in echoes from 1,500 to 2,100 km with stronger intensities at higher altitudes and lower background densities
- A plausible mechanism for lower hybrid waves in echoes involves a lower hybrid drift instability paired with an inverse energy cascade
- Several features of the echoes are consistent with the assumption that the irregularities originate from remnants of post-midnight ESF

**Correspondence to:**
S. Derghazarian,
sd779@cornell.edu

**Citation:**
Derghazarian, S., Rojas, E. L., Hysell, D. L., & Seyler, C. E. (2023). Lower hybrid waves in high altitude echoes of the topside equatorial ionosphere. *Journal of Geophysical Research: Space Physics*, *128*, e2022JA031036. https://doi.org/10.1029/2022JA031036

Received 23 SEP 2022
Accepted 24 JAN 2023



**Abstract** We investigate the mechanism underlying lower hybrid waves associated with high altitude echoes recently detected in the post-sunset equatorial topside ionosphere and inner plasmasphere by the Jicamarca VHF radar. These waves are visible as prominent sidebands in the echo Doppler spectra. New experimental results and newly processed incoherent scatter radar (ISR) datasets are presented that provide clues as to the conditions in which the echoes and associated waves occur. Numerical simulations are presented which demonstrate the feasibility of an inverse energy cascade coupled with a short wavelength instability, that is, the lower hybrid drift instability, in explaining the waves. An inverse cascade is required for short wavelength lower hybrid waves to extend to the 3 m wavelengths measured by the Jicamarca radar. The simulations were able to reproduce some features of the measurements including the lower hybrid sidebands at 3 m wavelengths, asymmetry in the sidebands, and the damping effect of higher densities and lower altitudes.

## 1. Introduction

High altitude echoes are topside or lower plasmaspheric coherent echoes that have been observed at altitudes between 1,000 and 2,200 km above Jicamarca and occur mainly in the postmidnight and predawn sectors (Derghazarian et al., 2021; Hysell et al., 2019). Their morphological and spectral characteristics are different from ESF. They are characterized by thin layers rather than convective plumes, and they exhibit spectral sidebands at the lower hybrid frequency.

Two processes thought to generate lower hybrid waves in the ionosphere, the lower hybrid drift instability (LHDI), and linear mode conversion of VLF whistlers via density depletions found in lower hybrid solitary structures (LHSS), were described in Derghazarian et al. (2021) as potential sources of lower hybrid waves in high altitude echoes. The LHDI in particular was shown to require the assistance of a cross-coupling mechanism for the instability to be able to excite lower hybrid frequencies at the 3 m wavelengths measured by the Jicamarca radar. Experimental evidence favoring one mechanism over the another is not definitive, however.

One argument favoring the LHDI is that it has shown promise as a potential source of low frequency irregularities in the equatorial *F* region. Kelley and McClure (1981) and Huba and Ossakow (1981a) argue that LHDI is the most likely explanation for 36 and 11 cm irregularities seen by the ALTAIR (Huba et al., 1978; Tsunoda, 1980) and TRADEX radars (Tsunoda, 1980), respectively, in conjunction with equatorial spread *F* (ESF). Apart from these studies, the theoretical treatments and reported measurements of the LHDI in the literature generally concern very low density, high temperature space plasmas such as at the magnetopause (Bale et al., 2002; Vaivads et al., 2004), in the magnetotail (Huba et al., 1978; Norgren et al., 2012), and at the plasmapause boundary (Mishin, 2013), but little is known about its prevalence in the equatorial inner plasmasphere.

The range of density gradient scale lengths ($L_n = (\nabla n/n)^{-1}$) present in the background plasma is a key factor that determines the frequencies produced by the LHDI. Experimental measurements of $L_n$ have been performed in the $O^+$ dominated *F*-region examined by Huba (1981) and Kelley et al. (1982) but such measurements are lacking in the inner plasmasphere.

If these gradients can become as steep as approximately half the proton gyroradius ($L_n \approx 1.5$ m) under some circumstances, along with the appropriate background plasma parameters, the LHDI can produce waves at the lower hybrid frequency with growth rates close to the maximum growth rate at the altitudes inhabited by the echoes. We argue in the text below that only for a narrow frequency band around the lower hybrid frequency, with waves that are of sufficient amplitude, and with wavenumbers that are not excessively large can the LHDI

trigger an inverse cascade and excite discernible 3 m wavelength LH waves. These conditions are satisfied when the background density is low (such as at low solar flux, high altitudes and in the post-midnight sector), and for magnetic field intensities that are sufficiently small such as those present in the upper range of altitudes at which the echoes manifest.

As for the ultimate source of steep plasma density gradients in the postsunset equatorial topside ionosphere, our working assumption is that these are provided by irregularities associated with postsunset equatorial spread *F*, a common phenomenon during low solar flux intervals. The characteristics of postsunset ESF and the most prolific theories regarding its origins were reviewed recently by Hysell et al. (2020). While there is still considerable uncertainty about the causes of postmidnight ESF, the widespread presence of irregularities in the postsunset topside over Jicamarca during low solar flux periods is certain.

This paper reports on numerical simulations of an inverse energy cascade powered by lower hybrid waves characteristic of the LHDI under the assumption of pre-existing, steep density gradients with scale lengths as described above. Several different wave amplitudes and wavenumbers are tested, and their effect on the inverse cascade is examined. We demonstrate that when the background plasma conditions described previously are satisfied (lower densities and weaker magnetic field intensities), both the LHDI and the inverse cascade can work together to produce discernible lower hybrid spectral sidebands at 3 m wavelengths. New experimental observations of the echoes along with newly processed information from archival ISR datasets are presented which support the simulation results.

## 2. Experimental Methods and Results

Two new types of experiments were conducted to investigate high altitude echoes at moderately low solar flux levels between June 2021 and January 2022 consisting of a combined long pulse and alternating code experiment and two alternating code experiments (Huba & Ossakow, 2000; Lehtinen & Häggström, 1987; Sulzer, 1993). High-altitude coherent echoes were detected in runs that occurred on 6–7 June 2021 and 28 January 2022, but the spectra lacked any detectable lower hybrid lines. The run on 24 October 2021 showed weak lower hybrid lines.

In addition to the two new experiments, archival data from routine topside ISR experiments were reprocessed to extract statistics regarding the presence of high altitude echoes at various solar flux levels, local times, and altitudes. The three long pulse/double pulse Faraday experiments described in Derghazarian et al. (2021) were also included. A spectral analysis was performed on the individual voltage samples of the data to search for lower hybrid waves. The sampling rate was 25 μs, and we used time series of 1 ms duration, yielding a bandwidth and spectral resolution of 10 and 1 kHz, respectively.

From a total of 18 days analyzed, high-altitude echoes were detected on 14 days. Most of the experiments were scheduled in the fall and winter so it is not yet clear whether the echoes present have seasonal variability. Table 1 is a summary of the findings from experiments from 2010 onward where echoes were observed, including the long pulse experiments performed from 21–24 October 2019 and described in the previous study on high altitude echoes. The date, time, altitude of occurrence of high altitude echoes, solar flux, and AP index as well as the characteristics of the associated lower hybrid lines are tabulated. Figure 1 displays information about the amplitude of lower hybrid waves present at various locations in range and time inside the echoes listed in Table 1. The panel on the left displays these locations in altitude and local time, and the panel on the right displays the same locations in terms of density and altitude. Densities are modeled using SAMI2-PE (Huba et al., 2000; Varney et al., 2012). Observations are binned into 100 km intervals starting at 1,000 km. As in Table 1, the intensity of the lower hybrid lines is subdivided into four categories depending on the number of decibels above the noise floor. Lower hybrid lines less than 3 dB above the noise floor are categorized as weak and shown in blue, from 3 to 6 dB as moderate and shown in orange, and larger than 6 dB as strong and shown in red. The absence of detectable lower hybrid lines inside the echoes is represented with empty black circles. The statistics included in the figures are limited to the post-midnight and pre-sunrise sector (00:00–04:30 LT) to restrict the analysis to periods of relatively constant temperature.

Several important points can be made from the data in the table and figures:

1. All echoes presented in this study were observed between 1,000 and 2,100 km altitude.
2. Locations in echoes with moderate and strong lower-hybrid lines (shown by orange and red circles) occurred in the upper altitude range at which the echoes manifest.

**Table 1**
*Summary of High Altitude Echo Statistics From 2010 to 2022*

| Date/LT (hhmm) | Altitude (km) | F10.7 | AP index | LH line intensity |
|---|---|---|---|---|
| December 10 2010; 01:00–04:00 | 1,800–2,000 | 84.5 | 10 | Strong |
| 12–13 July 2017; 02:30–03:30 | 1,800–2,000 | 95 | 4 | Strong |
| 23 January 2019; 23:30–01:00 | 1,200–1,800 | 70 | 10 | Undetectable |
| 16–17 October 2019; 01:00–04:00 | 1,800–2,000 | 66 | 5 | Weak |
| 21–22 October 2019; 20:00–07:00 | 1,500–2,100 | 65 | 5 | Strong |
| 22–23 October 2019; 03:30–05:30 | 1,200–1,500 | 64 | 5 | Weak |
| 23–24 October 2019; 03:30–05:30 | 1,100–2,100 | 64 | 20 | Strong |
| 18 February 2020; 00:30–02:00 | 1,500–2,000 | 69 | 15 | Undetectable |
| 19–20 February 2020; 22:00–02:00 | 1,000–2,000 | 69 | 10 | Moderate |
| 1–2 September 2020; 00:30–02:00 | 1,500–1,700 | 70 | 15 | Weak |
| 6–7 June 2021; 22:30–00:00 | 1,000–1,800 | 80 | 4 | Undetectable |
| 30 October 2021; 00:00–07:00 | 1,000–2,000 | 105 | 10 | Weak |
| 28 January 2022; 00:00–07:00 | 1,000–2,000 | 110 | 5 | Undetectable |

3. Locations in echoes that occurred in the low to mid altitude range had no or weak lower hybrid lines (shown by empty or blue circles) and were therefore characterized by a more intense background geomagnetic field.
4. All locations in echoes that occurred at modeled densities above $8 \times 10^9$ $m^{-3}$ had no or weak lower hybrid lines.

The observations strongly point to the absence of the lower hybrid lines in regions of higher magnetic field intensities corresponding to lower altitudes and also at higher densities as indicated in the right panel of Figure 1. There are some exceptions, but the trend is clear.

Figure 2 provides a closer look at the spectral characteristics of the echoes from 22 October 2019, for reference. The top panel displays the coherence of the echoes in range and time. The second and third panels show the

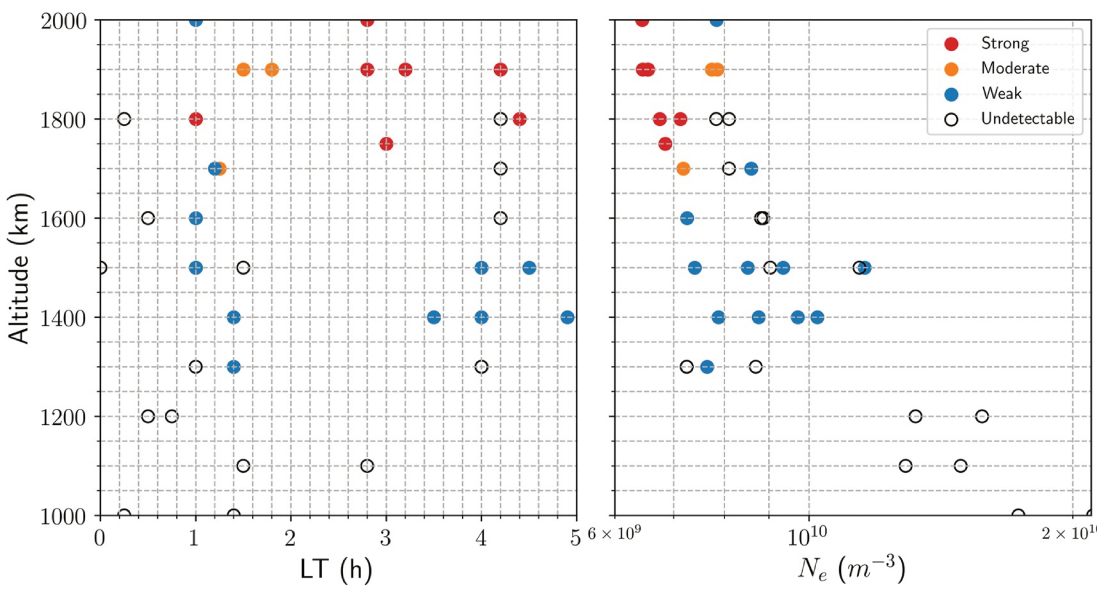


**Figure 1.** Statistical representation of multiple observation locations within high altitude echoes in terms of altitude, densities, and local time for the events in Table 1. SAMI2-PE (Huba et al., 2000; Varney et al., 2012) was used to model background density based on solar flux index and day of year. The left panel represents statistics of these locations in terms of altitude and local time, and the right panel their distribution in terms of altitude and modeled densities. Different colors represent varying intensities of lower hybrid lines inside the high altitude echoes, with red being the strongest and blue the weakest. Points inside the echoes where no lower hybrid line were detected are represented by open black circles.

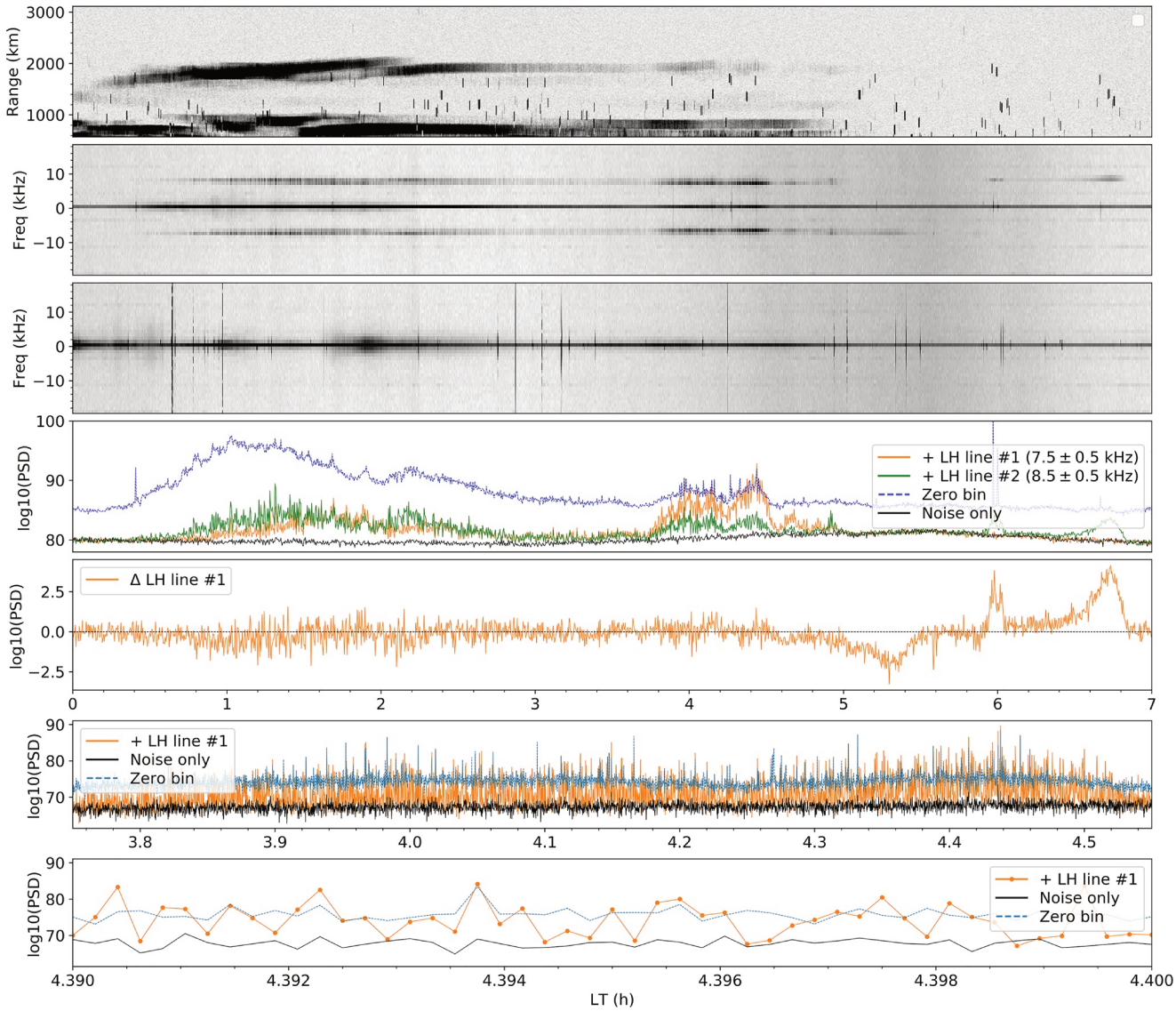


**Figure 2.** High altitude echoes observed on 22 October 2019 from an experiment conducted at Jicamarca with the 50 MHz VHF radar. The top panel depicts the coherence of the echoes in range and time. The second and third panels show the spectrograms at fixed altitudes of 1,800 and 800 km in the echoes respectively. The fourth panel displays the two most prominent lower hybrid lines and the zero frequency bin. The fifth panel shows the amplitude difference between one of the positive and negative lower hybrid sidebands. The sixth panel is a high time resolution plot of one of the lower hybrid lines, the zero bin and a bin without a signal that represents the noise floor. The bottom-most panel is an exploded view of a small region in the panel immediately above which shows the time scale of the small amplitude oscillations of the lower hybrid wave.

spectrograms at fixed altitudes of 1,800 km in the echoes, and 800 km in the lower altitude ESF structure respectively. LH sidebands are only observed in the second panel associated with high altitude echoes. The presence of faint lines at $\approx\pm 11$ kHz and $\pm 2$ kHz in both the spectrograms is due to artifacts, and it can be observed that the lines are identical despite being associated with time series that are thousands of km apart. The fourth panel compares two consecutive lower hybrid lines with positive frequencies in relation to the central line (blue). In addition, the positive and negative lower hybrid sidebands in the spectrogram are generally unequal in amplitude, and the fifth panel displays the amplitude difference versus time. The sixth panel shows a higher time resolution (750 ms) snapshot with the black line at the bottom indicating the noise floor, the blue line the center frequency bin, and the orange line the lower hybrid wave. This panel indicates that the amplitudes of the lower hybrid lines fluctuate between a given value and the noise floor whereas the center line only contains small amplitude fluctuations at the same level as the noise. This behavior of the LH lines, along with the fact that it is not observed elsewhere in the spectra, suggests that the production of lower hybrid waves is associated with an underlying

instability with rapid growth and decay phases. The average period of this growth and decay is comparable to the time resolution in the last panel of Figure 2 which is 750 ms.

## 3. Review of the Lower Hybrid Drift Instability

This section will focus on a theoretical review of the lower hybrid drift instability and its expected behavior in the post-midnight equatorial inner plasmasphere. By evaluating the appropriate dielectric tensor, with the assumption of density gradients of short scale length ($L_n \approx 1.5$ m), we will identify the background conditions required to produce lower hybrid pump waves capable of exciting an inverse energy cascade. The results of the simulation, which will be presented later on in this study, indicate that an inverse cascade can only be triggered by pump waves near the lower hybrid frequency with sufficient amplitude and duration (or sufficient energy).

The electrostatic form of the LHDI occurs when the ion diamagnetic drifts (due to density and temperature gradients) couple with the drift wave modes of the plasma, imparting to the waves a positive growth rate through inverse Landau damping (Huba & Ossakow, 1981b). These drift modes arise as solutions to the dispersion relation derived by solving Vlasov's equation with the assumption of a non-uniform plasma (Hasegawa, 1975). The inhomogeneity of the density is incorporated into the derivation through the unperturbed electron distribution function (Huba et al., 1990). Furthermore, when $kL_n \gg 1$, the weak inhomogeneity approximation may be used to expand the distribution function locally and simplify the analysis. This approximation is valid for this study for $L_n \approx 1.5$ m since maximum growth typically occurs for $k \geq 20$ m$^{-1}$ for the conditions present in the inner plasmasphere and topside ionosphere. Although the drift waves can have electromagnetic components and propagate at different angles relative to $B$, the solutions that we examine here are electrostatic and propagate perpendicular to $B$ (flute modes).

Huba et al. (1990) developed an expression for the dielectric tensor of a sub-Alfvenic inhomogeneous plasma which incorporates electromagnetic effects, gravity, and neutral collisions. To evaluate the growth rate and dispersion relation for the LHDI, the expression given by the authors can be simplified by neglecting electromagnetic effects (since the plasma beta: $\beta \approx 10^{-6}$ in our case) and neutral collisions as well as setting the gravity induced drifts to zero. The effect of neutral collisions was examined and found to be negligible. The simplified form of this expression then yields the following longitudinal projection of the dielectric tensor:

$$D_{\phi\phi} = 1 + \frac{2w_{pi}^2}{k^2 v_{thi}^2}(1 + i\omega G_i(\omega, k, v_{di}, w_{ci}, \rho_i)) + \frac{2\omega_{pe}^2}{k^2 v_{the}^2}\frac{\omega_1 - \omega_2 B_1(k, \rho_e)}{\omega_1} \quad (1)$$

where the $G_i$ term represents the Gordeyev integral, and depends on the frequency, wavenumber, ion diamagnetic drift, ion gyrofrequency and ion gyroradius; $\omega_1 = \omega - kv_{di}$, and $\omega_2 = \omega - 2kv_{di}$ are Doppler shifted frequencies in the $y$-direction due to the ion diamagnetic drift; and $B_1$ is a Bessel function integral described in the Appendix of Huba et al. (1990) which depends on the wavenumber and electron gyroradius. The effect of density gradient scale lengths described earlier enters via the diamagnetic drift ($v_{di}$) which affects the $\omega_1$, $\omega_2$, and $G_i$ terms. Here, the ion diamagnetic drift is given by $v_{di} = -\frac{K_b T}{eL_n B}$ where $K_b$ is Boltzmann's constant, and the scale length, $L_n = \left(\frac{\nabla n}{n}\right)^{-1}$.

Figure 3 evaluates the frequencies and growth rates of the LHDI for conditions relevant here by solving Equation 1. The top panel shows the real frequency as a fraction of the local lower hybrid frequency ($\omega_r/\omega_{lh}$), and the bottom panel illustrates the growth rate as a fraction of the local lower hybrid frequency ($\gamma/\omega_{lh}$) for the root of $D_{\phi\phi} = 0$ (Equation 1). The solution is solved numerically for various altitudes as a function of wavenumber for $L_n = 1.5$ m. The local lower hybrid frequency ($\omega_{lh}$) was calculated using the perpendicular lower hybrid wave kinetic dispersion relation given in Baumjohann and Treumann (1996) by:

$$\omega^2 = \omega_{LH}^2\left[1 + \frac{3}{2}\left(1 + \frac{\omega_{pe}^2}{\omega_{ce}^2}\right)k_\perp \lambda_{Di}^2\right] \quad (2)$$

where $\lambda_{Di}$ is the Debye length and where $k_\perp = k$. As mentioned previously, this study is limited to lower hybrid waves that are exactly perpendicular to $B$.

The background temperature is set to 800 K, and densities are modeled using SAMI2-PE (Huba et al., 2000; Varney et al., 2012) for a solar flux index F10.7 = 69, and a fixed local time of 03:00 LT in the example shown

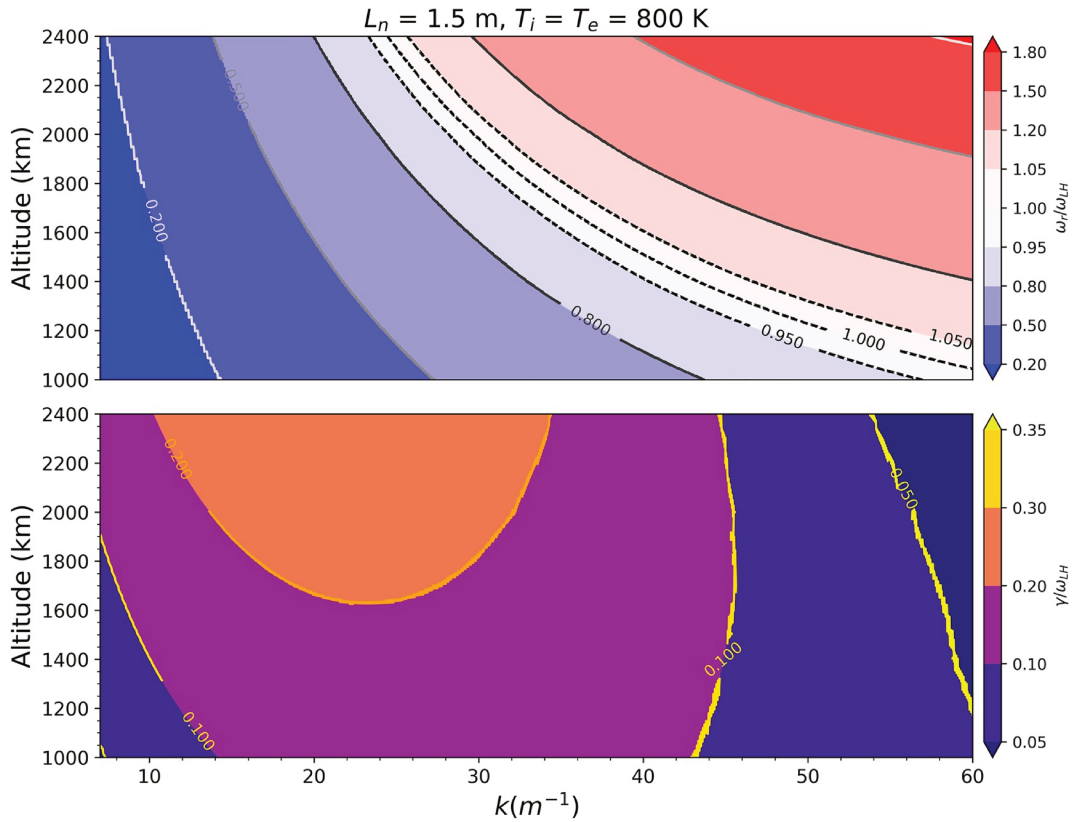


**Figure 3.** LHDI frequency and growth rate for a density gradient scale lengths of $L_n$ = 1.5 m as a function of altitude and wavenumber. The temperature is set to $T_e = T_i$ = 800 K. The figures illustrate a case where the solar flux index is F10.7 = 69 and the time is 03:00 LT. The top panel represents the ratio of real frequency to the local lower hybrid frequency, and the contour line with a value of unity (middle dashed line) represents the local LH frequency. The adjacent dashed lines delimit the area where the frequencies are within 5% of the LH frequency. Wavenumbers decrease and growth rates increase with altitude due to lower densities and magnetic field intensity. The bottom panel represents the ratio of the growth rate to the lower hybrid frequency.

in Figure 3. Magnetic field values are derived from IGRF-13 (Alken et al., 2021). Although this figure represents a single combination of local time and solar flux, it serves as a general qualitative example to understand the underlying mechanism.

The figure shows that waves produced at the lower hybrid frequency have growth rates close to the maximum at the highest altitudes but decrease with decreasing altitudes due to higher magnetic field intensity and background density. These waves are indicated by the unity contour (middle dashed line). Therefore, it is reasonable to assume that lower hybrid waves with weaker amplitudes are produced at lower altitudes. In addition, these waves have wavenumbers which increase with decreasing altitude.

Since in-situ measurements of LHDI amplitudes for the conditions of the inner plasmasphere are not available, experimental background LH wave amplitude statistics from other regions will be used as a proxy in this study.

In a recent large scale global statistical study of lower hybrid waves in the inner magnetosphere (Liu et al., 2021), wave amplitudes of 0.02–0.2 mV/m on average were observed in the equatorial plasmasphere and magnetosphere via the Van Allen probes in $L$-shells ranging from $L$ = 1.6–6. However in Berthelier et al. (2008), equatorial lower hybrid solitary structures (LHSS) in the $F$-region at altitudes of 700 km were found to exhibit electric field bursts of up to 15 mV/m. Despite the fact that the mechanism involved in the current study is different than that found in LHSSs, and statistical studies of LH wave amplitudes could not be found for the $L$-shells relevant to high altitude echoes, we nevertheless based the amplitudes of the lower hybrid pump waves in our simulation on values similar to those described above.

The duration of the waves also affects the inverse cascade coupling process, as will be seen in the simulations, but this will not be explored in detail in this study other than to note that a longer duration of the lower hybrid pump wave is required for weaker amplitudes to trigger an inverse cascade. In addition, because fluctuations are seen in all datasets (see e.g., Figure 2), it is likely that intermittent LH waves of finite duration are produced by the LHDI. One factor that could contribute to these fluctuations is an interplay between anomalous diffusion, which dissipates the gradients, and new irregularities drifting or emerging in the same volume, which acts to replenish them. In general, drift instabilities tend to destroy the density gradients that cause them through anomalous diffusion (Huba, 1981). The steeper the gradients, the shorter their lifetime, since the diffusion time is proportional to a power of the diffusion length.

## 4. Numerical Simulations

A numerical simulation of an inverse energy cascade was conducted to demonstrate the feasibility of the cross-coupling mechanism mentioned previously. The effect of the forcing amplitude and wavenumber of lower hybrid pump waves on the inverse cascade process, and consequently on the intensity of lower hybrid waves at 3 m wavelengths, is evaluated.

### 4.1. Inverse Cascade Theory

According to Kraichnan (1967), for 2D incompressible hydrodynamical turbulence, the root mean squared kinetic energy and vorticity are inviscid invariants of motion. They can be expressed in $k$-space as a function of wavenumber and have different power-law dependencies.

Similarly, it can be shown that the electrostatic two-fluid model given in Seyler (1994) which forms the basis of the simulation model in this study, possesses two quadratic invariants ($\mathcal{E}$ and $\Gamma$) that can be expressed as follows:

$$\begin{aligned} \mathcal{E} &= \int dx^2 \left[\Omega_i |\nabla\phi|^2 + \Omega_e |\nabla\chi|^2\right] \\ \mathbf{\Gamma} &= \int dx^2 \left[\Omega_i |\nabla^2\phi|^2 + \Omega_e |\nabla^2\chi|^2\right] \end{aligned} \tag{3}$$

In Fourier space, they take on the following form:

$$\begin{aligned} \mathcal{E} &= \sum_k \mathcal{E}_k = \sum_k k^2 \left[\Omega_i |\phi|^2 + \Omega_e |\chi|^2\right] \\ \mathbf{\Gamma} &= \sum_k \Gamma_k = \sum_k k^4 \left[\Omega_i |\phi|^2 + \Omega_e |\chi|^2\right] \end{aligned} \tag{4}$$

where $\chi$ is the curl free ion velocity potential, and $\phi$ is the perturbed parallel magnetic field which is related to the electron velocity through the relation: $u_e = \frac{1}{n_0 e \mu_0} \hat{z} \times \phi$. As proposed in Kraichnan (1967), for the inviscid invariants of motion to be simultaneously conserved, when an external forcing band of energy is injected into the system at an intermediate wavenumber $k_F$, it must be accompanied by a forward cascade of the second invariant $\Gamma_k$ (root mean squared vorticity) in $k$-space toward higher wavenumbers and an inverse cascade of the first invariant $\mathcal{E}_k$ (root mean squared kinetic energy) in $k$-space toward lower wavenumbers. This is the result of the different wavenumber dependencies of the invariants. As explained by the author, the energy spectrum of the first invariant follows a $k^{-5/3}$ law in the inverse cascade inertial range whereas the spectrum of the second invariant obeys $k^{-3}$ in the forward cascade inertial range. Simultaneous conservation of the invariants then requires the one with the steeper slope to cascade in the forward direction accompanied by an inverse cascade of the other invariant in the opposite direction.

Although the theory was developed for neutral fluids, the simulation results in this study show that it can also apply to the two fluid plasma even though the spectra of the invariants in $k$ space differ from that predicted in Kraichnan (1967).

An inverse cascade would then transfer the kinetic energy absorbed from a short wavelength (large wavenumber) pump wave at the lower hybrid frequency to lower hybrid waves at longer 3 m wavelengths (smaller wavenumbers $k = 2\pi/3$ m$^{-1}$). In addition to the kinetic energy, the density fluctuations are also transferred to longer wavelengths (smaller wavenumbers).

### 4.2. Inverse Cascade Model

The simulation model was derived from a modified version of isothermal two-fluid equations along with Ohm's Law, Faraday's Law, and Ampere's Law in which equal ion and electron temperatures ($T_e = T_i$) and quasi-neutrality are assumed. It is similar to the model described by Equations 6–9 in Seyler (1994), the main differences being that we take the electrostatic limit, consider only waves in the plane perpendicular to $B$, and introduce an external forcing function that acts as a proxy for the lower hybrid waves produced by the LHDI. Furthermore, the model considered here is cast in dimensional variables, accounts for background density and temperature, and includes electron-ion Coulomb collision terms. A review of the assumptions invoked in its derivation are given below and restate (Seyler, 1994). For further details on the derivation of the more general model including electromagnetic terms, off-perpendicular magnetic aspect angles, and density gradients, the reader may consult (Seyler, 1991, 1994).

Because the frequency of lower-hybrid waves falls in between the ion and electron cyclotron frequencies ($w_{ci} \ll w_{lh} \ll w_{ce}$), it is allowable to use the unmagnetized approximation for the ions, that is, to consider they are following straight line orbits, and to treat the electrons as strongly magnetized. The wavelengths considered in the model are much longer than the Debye length and the electron gyroradius which limits the maximum $k$ value to 80 $m^{-1}$ which is sufficient. The model consists of three equations: an electron dynamical equation and modified ion momentum and ion continuity equations. The first equation (Equation 5 below) is derived using Ohm's Law substituted into Faraday's Law which allows the electric field term to be eliminated. Nonlinear terms are retained in this equation up to second order only with the assumption that the parallel magnetic field ($B_0$) and density perturbations ($\delta_n$) are much smaller than the background values. The ion equations (Equations 5 and 7 below) are derived using the ion continuity and momentum equations in which the electric and magnetic field terms are also substituted using Ohm's Law. Ion non-linearities are ignored since the ion fluid velocity is assumed to be small compared to the ion acoustic velocity (Seyler, 1994). A simplified expression for the magnetic field is used which considers only the background magnetic field and the parallel perturbations. The transverse magnetic field perturbations are ignored since they lead to higher-order non-linear terms in the equations.

To simplify the analysis further, density gradients in the plasma are not considered, which is in contrast to the previous section where they were an important component in the derivation of the LHDI. The effect of these gradients is the addition of a second Hall term which affects the dispersive properties of the system, but the effects will be left for a future study.

The system variables are the curl free ion velocity potential ($\chi$), the perturbed parallel magnetic field ($\phi$) and the density ($n$). Using the first two of these terms instead of ion and electron velocities allows the system to be expressed in scalar form. The final dimensional model is shown in Equations 5–7 below, with the first equation pertaining to electron dynamics, and the second and third to ion dynamics.

The equations are as follows:

$$\partial_t \nabla^2 \phi + \frac{1}{n_0 e \mu_0} \hat{z} \cdot \left( \nabla \phi \times \nabla \nabla^2 \phi \right) = \frac{n_0 e^2 \mu_0 B_0}{m_e} \nabla^2 \chi + \mu \nabla^4 \phi - \nu_{ei} \nabla_\perp^2 \phi \tag{5}$$

$$\partial_t \chi = -\frac{B_0}{n_0 m_i \mu_0} \phi - c_s^2 \frac{n}{n_0} + \frac{e}{m_i k_x} F(k_x, \omega, t) \tag{6}$$

$$\partial_t \chi + n_0 \nabla^2 \chi = 0 \tag{7}$$

Here, $\phi$ represents the perturbed parallel magnetic field, $\chi$ the ion velocity potential, and $F = E_0 \sin(k_x - \omega_{lh} t)$ the forcing function. Also, $c_s = \sqrt{\frac{K_b (T_e + T_i)}{m_i}}$ is the ion acoustic speed, and $n = n_0 + \delta_n$ is the total density including the background field and perturbations. Furthermore, the ion velocity is given by $\nabla \chi$, the electron velocity by $u_e = \frac{1}{n_0 e \mu_0} \hat{z} \times \nabla \phi$, and the total magnetic field by $B = B_0 + \phi$. The collision frequency is given by $\nu_{ei} = \frac{54.5 \times 10^{-6} n_0}{T_e^{3/2}}$ (Schunk & Nagy, 2008).

The second term on the left side of Equation 5 contributes to the nonlinear evolution of the system and is the most important term in triggering the inverse cascade mechanism. The first term on the right side of Equation 5

**Table 2**
*Simulation Parameters*

| Parameter | Value |
|---|---|
| Grid size | $256 \times 256$ |
| Box size | $2\pi$ m |
| $B$ | $1.20 \times 10^{-5}$ T |
| $n_0$ | $8 \times 10^{9}$ m$^{-3}$ |
| $m_i(H^+)$ | $9.67 \times 10^{-27}$ kg |
| $m_e$ | $9.103 \times 10^{-31}$ kg |
| $T_e$ | 800 K |
| $T_i$ | 800 K |
| $dt$ | $5 \times 10^{-7}$ s |
| $T_{sim}$ | 500 ms |

couples the ion velocities to the electron dynamical equation and sets the eigenfrequency of the system to the lower hybrid frequency. Electron-ion Coulomb collisions were first inserted via a resistive term in Ohm's Law prior to derivation which then resulted in the rightmost term seen in the electron equation. The effect of Coulomb collisions on the ion momentum equation was considered negligible. The collision frequency term used was provided by Schunk and Nagy (2008).

An electric field perturbation (lower hybrid pump wave) of the form $E_0 \sin(k_x x - \omega_{lh} t)$ was introduced into the system via Ohm's Law which couples to the ion momentum equation resulting in the last term on the right side of Equation 6. A forcing band of waves was injected with a wavenumber spread of $k_x \pm 1$ m$^{-1}$ and a frequency spread of $f_{LH} \pm 5\%$ in order to mimic the range of wavenumbers and frequencies seen in the LHDI (Figure 3). The form of the forcing function is as follows: $F = E_0[\sin((k_x - 1)x - 0.95\omega_{lh}t) + \sin(k_x x - \omega_{lh}t) + \sin((k_x + 1)x - 1.05\omega_{lh}t)]$. For the purpose of this study, we consider $k_y = 0$ and the reasoning behind this is explained at the end of this section. Adding a larger number of adjacents wavenumbers and frequencies is possible, but doing so does not change the results of the simulation. This is because the associated frequencies move away from the LH frequency or from the eigenfrequency of the system, and have a negligible effect on the inverse cascade process.

Two different amplitudes were used for the pump waves: one at 20 mV/m, and another at 20 μV/m which largely overlap the range of values observed by satellite data in the lower *F*- region and higher *L*-shells in the plasmasphere as described in the previous section. In addition, the waves were windowed in time by a square pulse to limit their length to a 100 μs and 100 ms, respectively. The duration of the waves in this study is arbitrary and was kept as short as possible but sufficiently long to trigger the non-linear behavior of the system. The pulses were also windowed in time to mimic the fluctuating amplitudes seen in the experiment and observe the decay phase that follows the withdrawal of the pulse.

The viscosity term, the second term on the right side of Equation 5 in the simulation model, was calculated using the magnitude of the stress tensor (Schunk & Nagy, 2008) but little effect was noted on the results of the simulation. Its addition was important from a numerical standpoint to avoid the accumulation of excess energy at higher wavenumbers.

The simulation was performed using a spectral solver, Dedalus Project (Burns et al., 2020), which comes as a Python package. A two dimensional box was constructed with dimensions $2\pi \times 2\pi$. The gridding uses a Fourier base, periodic boundary conditions, and a grid size of $256 \times 256$. The parameters used are summarized in Table 2. Results were unaffected when larger grid sizes, simulation boxes, and shorter time steps were used, as long as the spectral bandwidth in $k$ space was kept equal to or larger than the current one. The sampling rate of $5 \times 10^{-7}$ s used was several times the period of lower hybrid waves and is short enough to avoid violating the CFL condition with the velocities present in the simulation. The grid dimensions provided the ability to resolve wavelengths from 25 cm–6.3 m or wavenumbers from $k = 1$ m$^{-1}$ to $k = 128$ m$^{-1}$. The system was initialized by setting the total density to the background density superimposed with random fluctuations with an amplitude of 0.1% of the background value. The ion velocity potential, the magnetic field perturbations, and the superimposed electric field perturbations (forcing function) were all initialized to zero.

The physical and spectral quantities of the simulation were derived from the density perturbations ($\delta_n$), as this is the appropriate variable to consider for comparing to radar echoes. The length of the simulations was limited to 500 ms by which time the most important features of the system were apparent.

Since the simulation results are generally isotropic and the simulation is performed in the 2*D* plane perpendicular to the magnetic field, any direction in this plane can be taken to correspond to the radar line of sight in the experiment. We have arbitrarily chosen the $x$ coordinate in the simulation to correspond to the radar line of sight. Furthermore, the lower hybrid pump waves were injected in the $x$-direction assuming $k_y = 0$. Runs in which $k_y \neq 0$ did not produce a significant difference in the results. The choice of this direction of injection is to simplify the analysis but is otherwise arbitrary. This is motivated by the fact that the density gradients, diamagnetic drifts and

drift waves produced by the LHDI are unlikely to be preferentially oriented in the plane perpendicular to $B$. In addition, the analysis in this study is restricted to LH waves with $k_{\parallel} = 0$, but experimental measurements of a $k_{\parallel}$ component and numerical simulations that investigate the contribution of this component to the overall results will need to be investigated in a future study.

The plasma parameters shown in Table 2 were used throughout all simulation runs, as the results showed little sensitivity to changes of these parameters within their range of variability for the conditions of this study. The different simulation runs were therefore solely focused on examining the effect of the pump wave amplitude and driving wavenumbers on the inverse cascade process. Since the ion composition at all altitudes where high altitude echoes manifest is almost exclusively dominated by $H^+$, the ion mass of a proton was used in all simulations. The presence of heavier ions acts to inhibit the production of LH waves but this will be left for a future study.

### 4.3. Simulation Results

The simulation can be roughly divided into three regimes: linear, non-linear with growing wavelengths, and non-linear with largely steady wavelengths.

Each regime is delimited by dashed vertical lines and identified by roman numerals in the first and fourth panels of Figures 4 and 5, and the bottom panel of Figures 6 and 7. Four different simulation runs are presented which investigate the result of coupling lower hybrid waves to an inverse cascade. For the first two runs we keep the wavenumber constant but vary the amplitude in order to examine the effect of the latter on the lower hybrid lines at 3 m wavelengths. A narrow band of wavenumbers ($k_x = 30 \pm 1$ m$^{-1}$) is chosen which is associated with lower hybrid waves generated by the LHDI at high altitudes (see top panel of Figure 3). The corresponding band of frequencies are 95%, 100%, and 105% of the lower hybrid frequency (see top panel of Figure 3). For the third and fourth runs (see Figures 8 and 9), the same amplitudes are used as those in Figures 4 and 5 respectively, but a higher band of wavenumbers ($k_x = 50 \pm 1$ m$^{-1}$) is used which is associated with lower hybrid waves produced by the LHDI at lower altitudes.

Figure 4 displays the results of a simulation performed for a lower hybrid pump wave of high amplitude and short duration ($E_0 = 20$ mV/m and $\Delta t = 100$ μs duration). The first panel of the figure displays the evolution of the background density perturbations averaged over the $y$ coordinate, versus $x$ and time. These values are normalized to their standard deviation along the $x$-axis at each time step so the color-scale of the plot can capture the evolution of the wavelengths clearly throughout the entire simulation. It is obvious from the figure that the dominant wavelength becomes progressively longer as the simulation evolves. The standard deviation is shown using a thin dotted blue line and represents the evolution of the perturbation amplitude. A rapid growth phase occurs following the injection of the pump wave at 20 ms and is followed almost immediately by a drop in amplitude after which the final value of the perturbation is reached around 100 ms and remains approximately constant until the conclusion of the simulation.

The second panel illustrates the spatial power spectrum of the density and signifies the evolution of the system in $k_x$-space for $k_y = 0$. Energy is injected through the band of wavenumbers and frequencies mentioned above and can be seen by the prominent red pulse in the figure at a time of 20 ms. The energy from the pulse can then be seen to cascade from the injection wavenumber band toward lower wavenumbers as the system evolves. Higher wavenumbers are damped by viscosity and diffusion at a rate proportional to their value and appear to have mostly dissipated by the second half of the simulation.

The third panel is a spectrogram constructed from the time series of the spectral amplitude for $k_x = 2\pi/3$ m$^{-1}$ ($\lambda = 3$ m), $k_y = 0$. A rolling time window of 1 ms with a sampling period of 10 $\mu$s was used to obtain spectral power quantities, thus providing a spectral resolution of 1 kHz and a bandwidth of 50 kHz. The fourth panel is a line plot showing the amplitude of the positive and negative lower hybrid sidebands from the panel above. Both sidebands grow rapidly after the system enters a non-linear growth phase that begins with the injection of the pump wave band and reach an amplitude eight to 10 orders of magnitude higher than present in the unperturbed system. Subsequently, both amplitudes drop slightly throughout the remainder of the simulation and by its conclusion are still seven orders of magnitude larger than the amplitudes prior to forcing. The bottom panel displays the power difference between the positive and negative LH sidebands.

Figure 5 demonstrates the result of a simulation in which the lower hybrid pump wave has an amplitude of just 0.02 mV/m (vs. 20 mV/m) and a duration of 100 ms (vs. 100 μs). The purpose of this example is to illustrate the

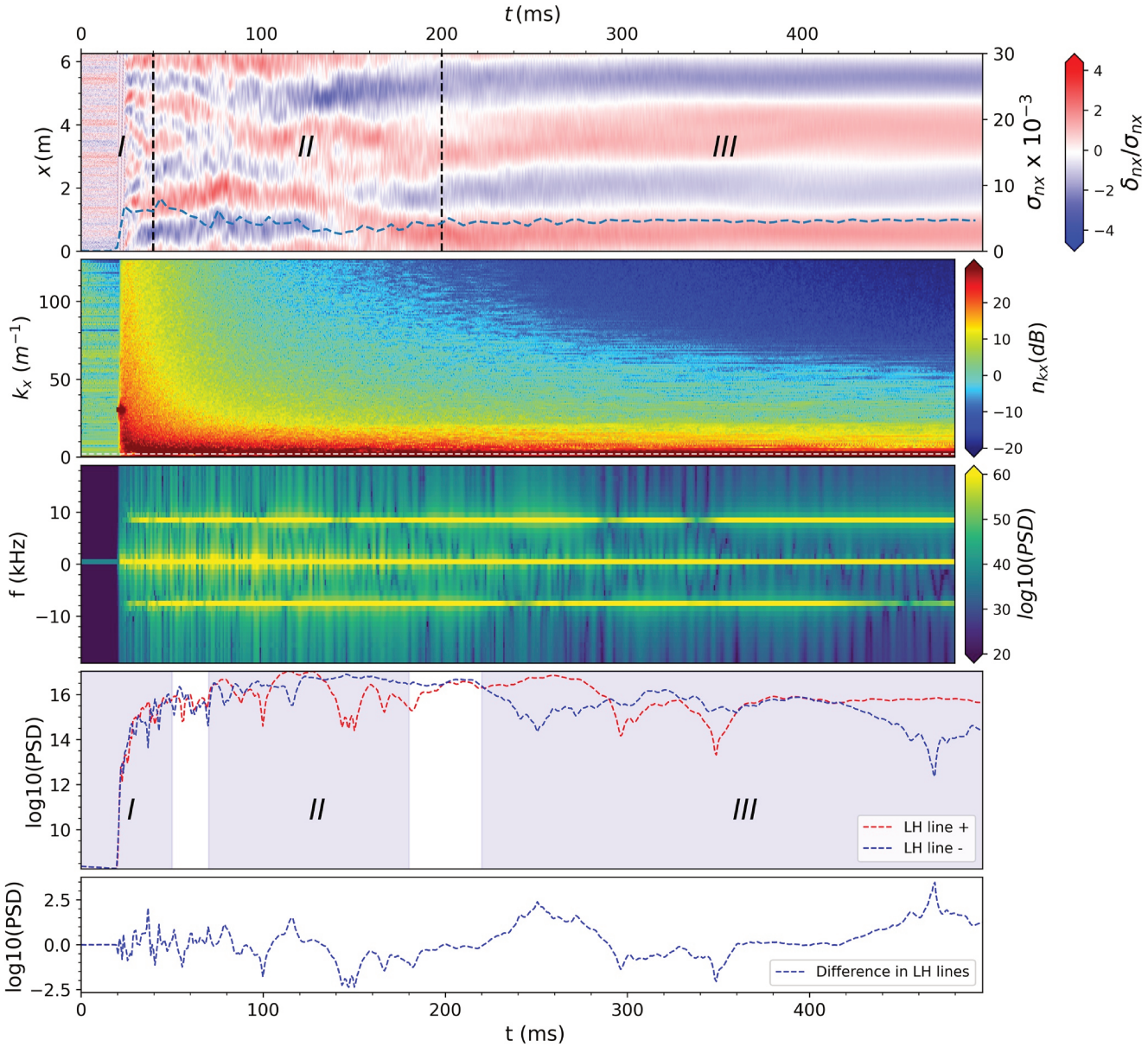


**Figure 4.** Simulation results using the parameters described in 1. The top panel displays $y$-averaged density variations across the $x$-axis. The second panel shows the spatial power spectrum of the density in the $k_x$ direction $(|n_{k_x}|^2)$. The pump waves that are injected into the system can be seen as a narrow band of three adjacent wavenumbers centered around $k = 30$ m$^{-1}$. The third panel represents a spectrogram of the density perturbations at a wavenumber $k_x = 2\pi/3$ m$^{-1}$, $k_y = 0$ which corresponds to a wavelength of 3 m. The fourth panel is a line plot of the positive and negative sideband amplitudes from the spectrogram above. The fifth panel displays the difference between the positive and negative lower hybrid sideband amplitudes.

effect of lower pump wave amplitudes on the intensity of LH waves at 3 m wavelengths. Larger wavelengths are excited as in the previous example and become dominant after approximately 200 ms. In the second panel, the cascading process is more gradual and the energy excited at lower wavenumbers shortly after the injection of the wave has lower amplitudes. The lower hybrid lines in the spectrogram represented by the third panel shows much weaker LH lines than in Figure 4. In the fourth panel, the maximum amplitude of these 3 m wavelength LH lines is only two to three orders of magnitude larger from its initial value instead of eight to 10 orders of magnitude as in the previous example.

Each column in Figure 6 corresponds to fixed times of 21 ms (1 ms after the injected pulse), 90 ms (the middle of the second regime) and 500 ms (end of the simulation), respectively. The three figures in the top row of Figure 6 represent the density structures in $x$–$y$ space for the same run as in Figure 4. The average RMS density value is

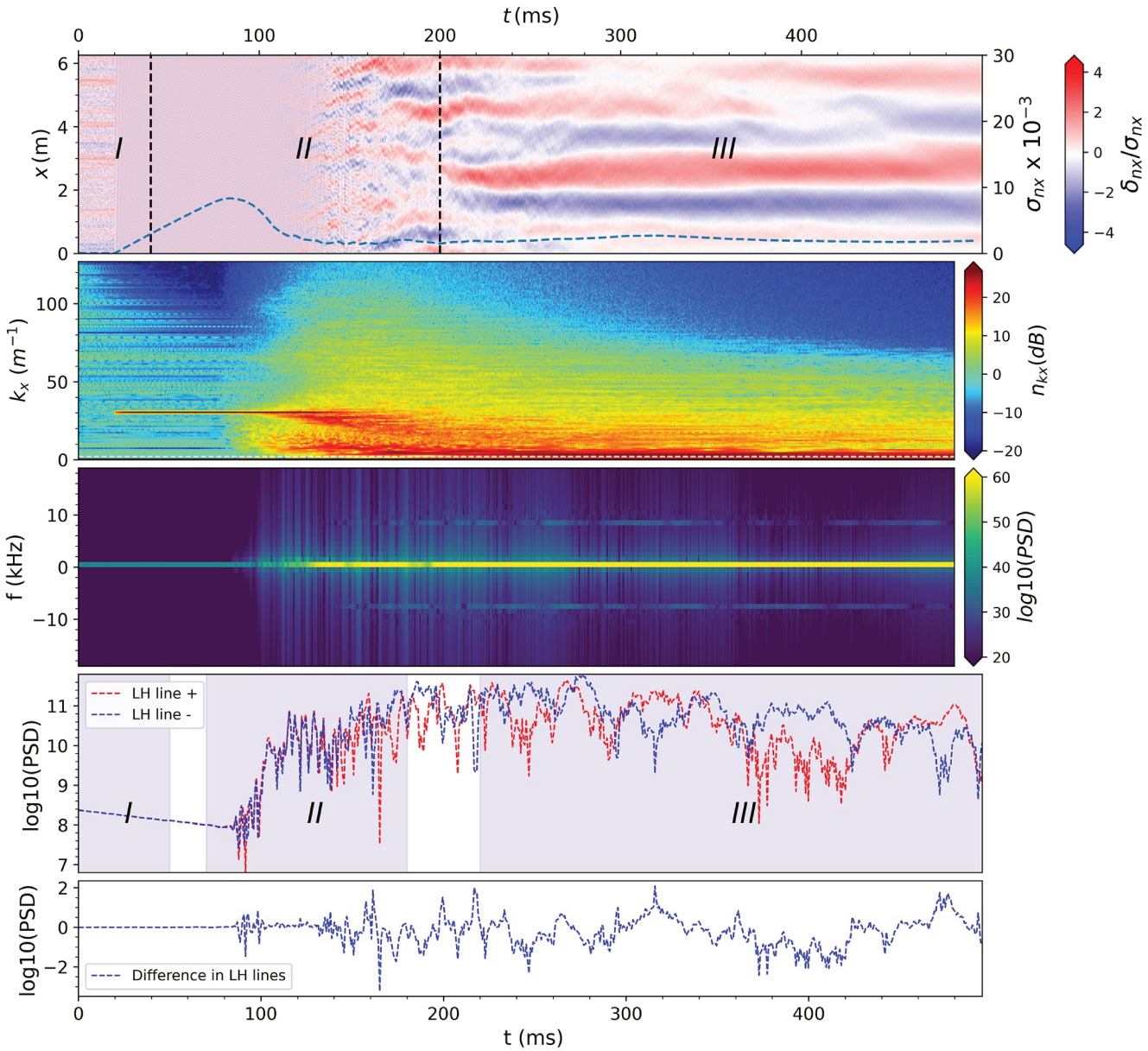


**Figure 5.** Same as above but with a forcing function of 0.02 mV/m instead of 20 mV/m. The amplitude of the LH lines and other frequencies decrease noticeably faster with simulation time.

printed in the upper portion of the plots. The amplitude of the density perturbations grows at first and then, as the system evolves further, diminishes. However, an interesting feature is that the dominant wavelength (wavenumber) of the density structures continues to increase (decrease) throughout, indicating that the inverse cascade operates continuously even as the energy in the system is diminishing with time due to collisions and diffusion.

The set of three figures in the second row provides evidence of the inverse energy cascade in the $k_x$–$k_y$ plane. The first plot illustrates the wavenumber injection band (delimited by a black dashed contour), accompanied by the excitation of surrounding $k_x$ and $k_y$ modes. In the second plot, which corresponds to the conclusion of the rapid growth phase, there is a spread of energy throughout all $k_x$ and $k_y$ modes but with larger amplitudes at longer wavelengths. In the third plot corresponding to the conclusion of the simulation, the highest energy concentration is in the lowest $k_x$ modes. If we compare the first and third plots, it is evident that the energy has cascaded from higher to lower wavenumbers. The bottom panel of Figure 6 displays the electron and ion RMS velocities and RMS electric field amplitudes present in the simulation.

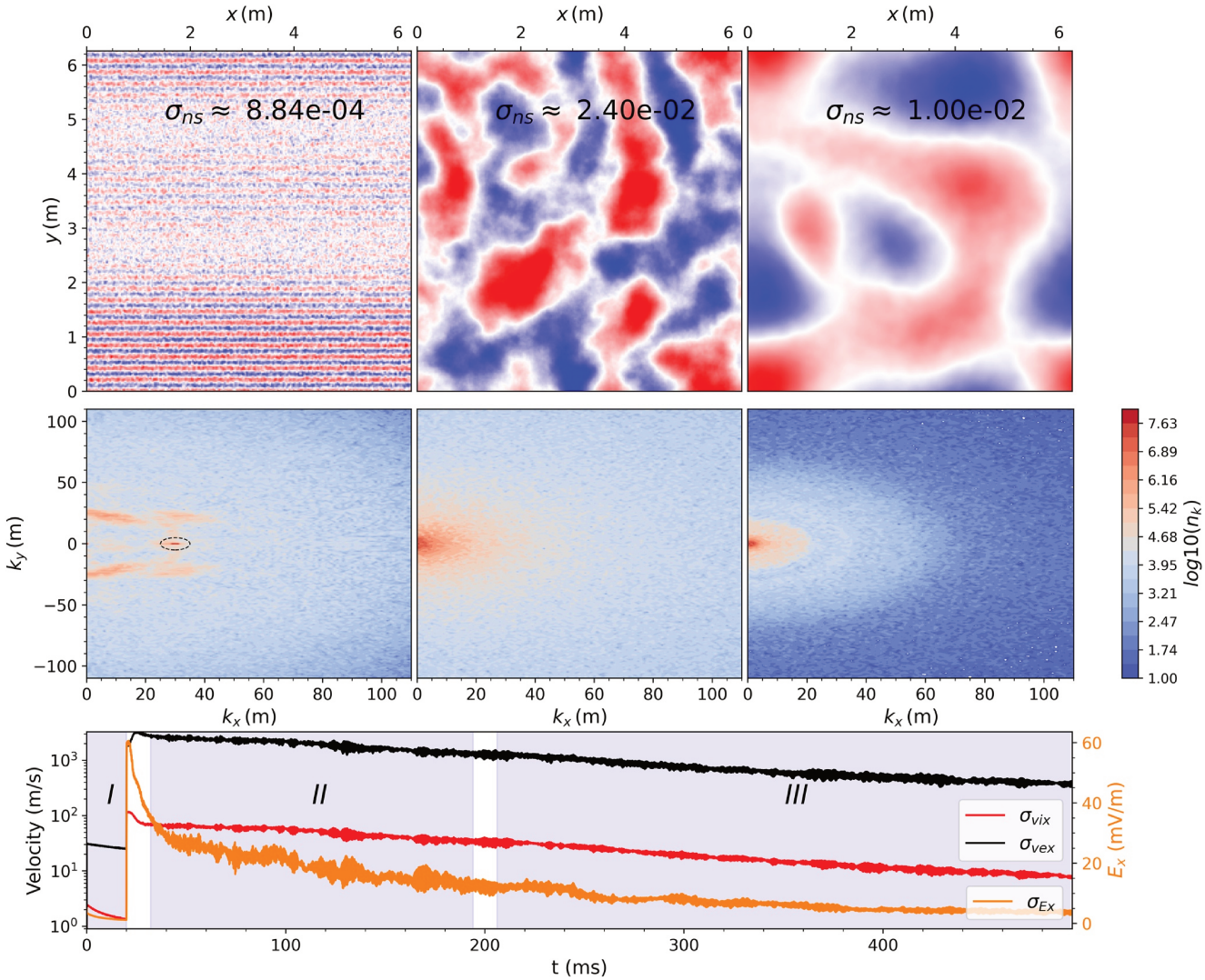


**Figure 6.** Spatial and spectral plots based on the same run as in Figure 4. The top three panel in the first row represent the density perturbations in the $x$–$y$ plane at three different time periods in the simulation (in the linear regime, the transition regime and non-linear regime). The next three plots in the second row represent the distribution of spectral energy in the $k_x$–$k_y$ plane. Both $k_x$ and $k_y$ represent the spatial PSD of the density irregularities. The bottom panel displays electron and ion velocities and electric field amplitudes in the $x$ direction for $k = 2\pi/3$ m$^{-1}$.

The electron velocities reach a peak of 1,500 m/s after the pump wave is injected to 200 m/s at the end of the simulation, whereas the ion velocities vary from 100 to 5 m/s. The electric field perturbations vary from 60 to 3 mV/m.

Figure 7 illustrates the evolution of density structures in the same manner as in Figure 6 but corresponds to the run in Figure 5 where the pump wave amplitude is three orders of magnitude lower. Each column corresponds to a fixed time of 100 ms (at the transition between the linear and non-linear regimes), 200 ms (the middle of the second regime), and 500 ms (end of the simulation), respectively. In contrast to Figure 6, the long wavelength structures have lower amplitude, and the spectral power at lower $k$ values is much weaker.

It was previously seen in Figure 3 that the driving wavenumbers of lower hybrid waves produced by the LHDI increase with decreasing altitudes. A comparison of Figures 5 and 8 provides evidence that increasing the wavenumber of the pump wave sufficiently while its other parameters remain fixed, suppresses the production of lower hybrid waves at 3 m wavelengths. Both the simulations were performed with low amplitude LH pump waves of 20 μV/m. Figure 8 shows that although an inverse cascade is still active for a wavenumber of $k = 50$ m$^{-1}$, the intensity of lower hybrid waves in the spectrogram of the same figure can be seen to have diminished considerably, and

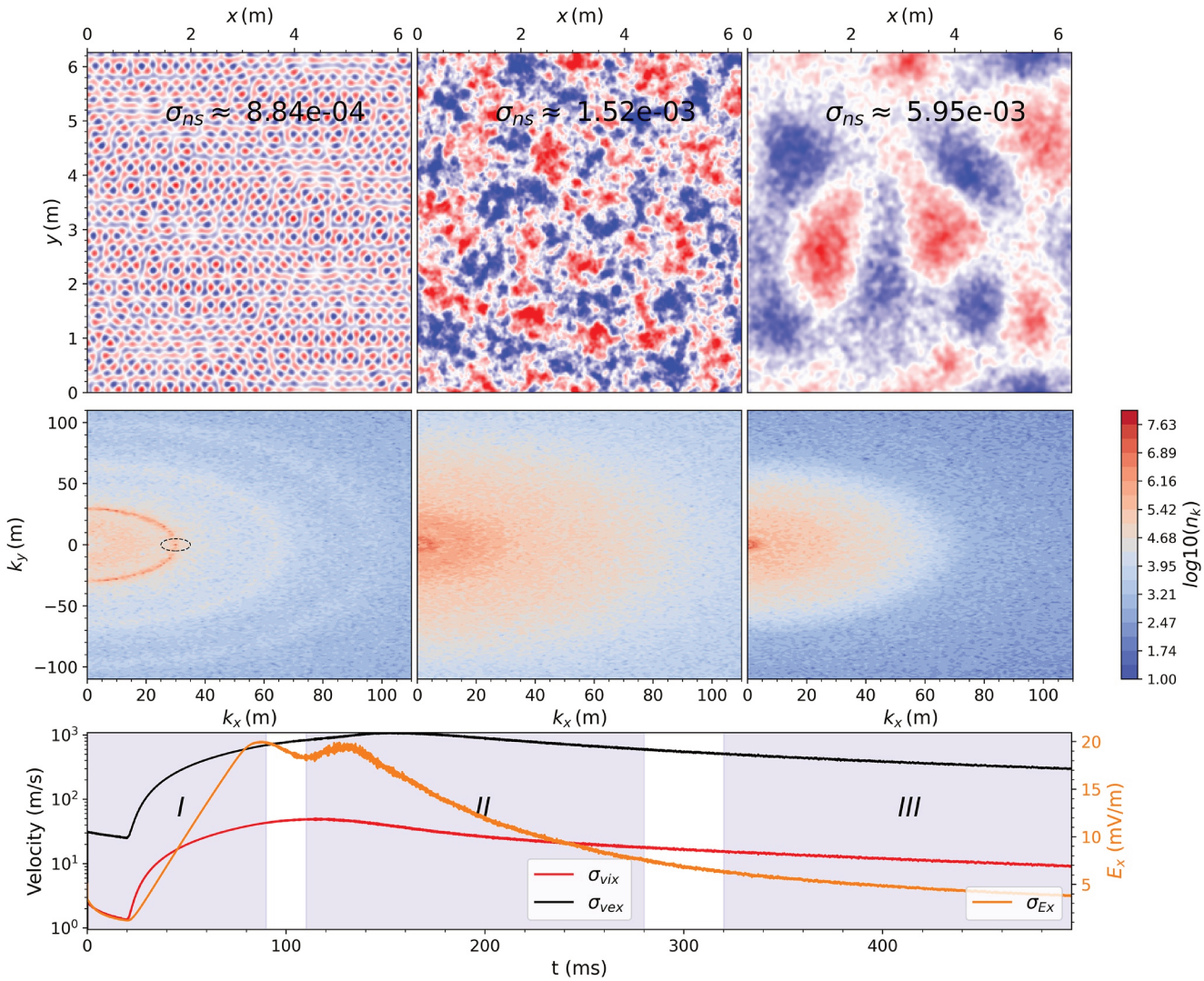


**Figure 7.** Spatial and spectral plots based on the same amplitude as in Figure 5 and with the same analysis as in Figure 6.

this will be increasingly so for larger values of $k$. The inability of waves to grow considerably at 3 m wavelengths in this case could potentially be the result of the inability of a large portion of the energy injected to get transferred to the lowest wavenumbers, which appears instead to remain confined in part to an area in $k$ space near the injection wavenumber (see second panel in Figure 8).

The effect of increasing the wavenumber of a large amplitude LH pump wave is illustrated in Figure 9. In this simulation, a LH wave is injected with a band of wavenumbers centered around $k = 50$ m$^{-1}$ and an amplitude of 20 mV/m which is equal to the one used in the first simulation (Figure 4). Despite the large amplitude of the pump wave, the LH sidebands at 3 m are weak and comparable to the case where $k = 30$ m$^{-1}$ and an amplitude of 20 μV/m was used (Figure 5). This result indicates that even at larger pump wave amplitudes, significant LH waves at 3 m are not produced when the injection wavenumber is too large.

To summarize, the salient features of the simulations are the following:

1. An inverse cascade is possible for a large interval of different LH pump wave amplitudes provided they are applied for a sufficiently long time interval. The cascade is visible in the second row of Figures 6 and 7 and can be identified by a movement of energy from the injection band to lower wavenumbers in the $k_x$–$k_y$ plane.
2. Large amplitude waves at the lower hybrid frequency were produced at 3 m wavelengths ($k = 2\pi/3$ m$^{-1}$) when a band of high amplitude (20 mV/m) sinusoidal pump waves were injected with wavenumbers (centered around $k = 30$ m$^{-1}$ in this example) and a narrow band of frequencies centered around the lower hybrid frequency.

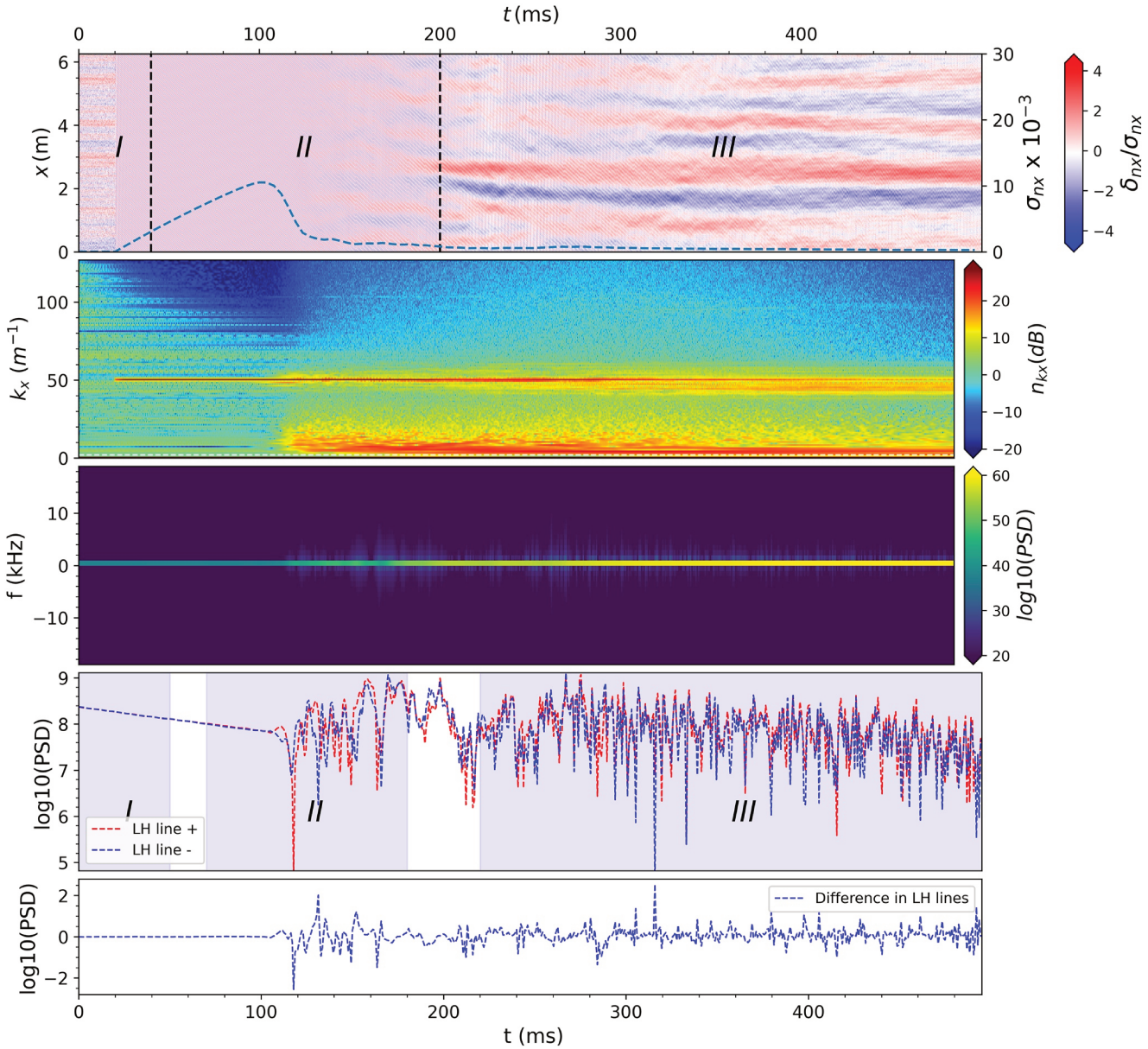


**Figure 8.** Same amplitude as in Figure 5 but with lower hybrid pump waves centered around $k = 50$ m$^{-1}$.

3. Lower amplitude LH waves at 3 m wavelengths ($k = 2\pi/3$ m$^{-1}$) are produced by very low amplitude LH pump waves provided the latter are applied for a longer duration. The amplitude of these pump waves are likely to be representative of weaker growth rates of the LHDI at lower altitudes.
4. Lower amplitude LH waves at 3 m wavelengths ($k = 2\pi/3$ m$^{-1}$) are produced by high amplitude and large wavenumber LH pump waves.
5. Negligible LH waves at 3 m wavelengths ($k = 2\pi/3$ m$^{-1}$) are produced by very low amplitude and large wavenumber LH pump waves characteristically produced by the LHDI at low altitudes.
6. Differences in the amplitudes of the LH sidebands can be seen throughout the simulation as indicated in the bottom panel of Figures 4 and 5.

## 5. Discussion

It was shown in the second simulation run that even if small amplitude waves are applied to the system as in Figure 5, they can excite an inverse cascade if they are of sufficient duration. This result indicates that, for a

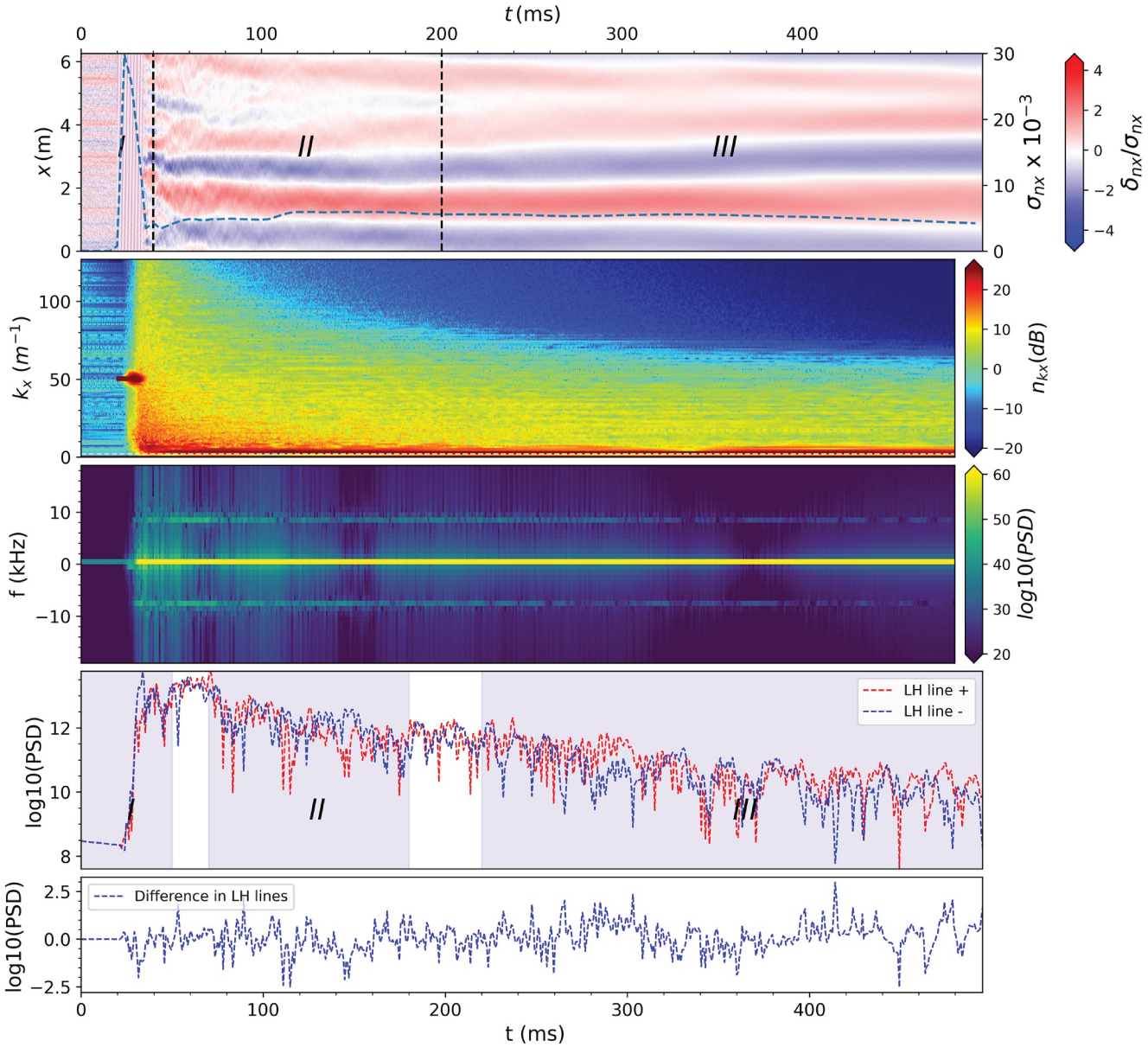


**Figure 9.** Same amplitude as in Figure 4 but with lower hybrid pump waves centered around $k = 50$ m$^{-1}$.

given wavenumber, a large range of lower hybrid pump waves with sufficient energy or the right combination of amplitude and duration can trigger an inverse cascade. However, it is clear that the intensity of the LH lines produced at 3 m is proportional to the pump wave amplitude. In Figure 3, since it was shown that the LH waves produced by the LHDI have lower growth rates at lower altitudes, that it would be reasonable to assume that this could explain in part why experimental LH lines are weaker at lower altitudes. Another factor to consider is the increased wavenumbers of LH waves produced by the LHDI at lower altitudes which leads to weaker 3 m LH waves via an inverse cascade.

From the experimental data shown in Figure 1, the role of the magnetic field intensity and background density in inhibiting lower hybrid lines in the backscatter has been made clear. According to the panels on the left and bottom of the figure, lower hybrid lines were undetectable or manifested weakly at higher density, and low altitudes, or a combination of both. The higher densities could be the result of low altitudes, elevated solar flux or earlier local times. Below approximately 1,200 km no lower hybrid lines were seen in the echoes, which appears to indicate a lower cutoff. This observation can be explained by the considerably more intense magnetic field

intensity and densities present which render the lower hybrid lines undetectable. There is no upper cutoff for the lower hybrid lines as long as the coherent echoes are present.

The role of temperature was not directly addressed in this study, but it can be noted that higher temperatures favor the inverse cascade mechanism by lowering the driving wavenumber of the lower hybrid pump waves. At earlier local times (22:00–00:00 LT), and at later local times (04:30–07:00 LT), discernible lower hybrid lines should be expected to appear at lower altitudes provided the appropriate scale lengths are present in the echoes.

In this study, density gradients with scale lengths of $L_n \approx 1.5$ m were assumed. If shorter scale lengths were present in sufficient quantity, the growth rate of the lower hybrid pump waves would be closer to its maximum value even at the lowest altitudes of the inner plasmasphere such that they would be able to strongly excite an inverse cascade and discernible 3 m wavelength lower hybrid lines at lower altitudes than those seen in the experimental data. The presence of much shorter density gradient scale lengths in sufficient quantity is thus unlikely.

Fluctuations in the LH lines produced by the simulation (Figures 4 and 5) appear at timescales of the order of several milliseconds. Those seen in the experimental data, on the other hand, are on a much longer timescale of 0.5–2 s (Figure 2). The simulation results cannot account for this aspect of the experimental observations, but an explanation is likely to be found in the LHDI process itself. In Figure 4, it was shown that a lower hybrid pump wave of short duration will trigger the growth of 3 m LH waves, and a decay phase will subsequently follow as soon as energy ceases to enter the system. The longer timescale for this process matches more closely the observations. Therefore, if the origin of the fluctuations can be traced to the LHDI itself, this could explain the observations in the data. Further investigation of the LHDI process is warranted.

On the other hand, the lack of visible fluctuations seen in the zero frequency bin of the experimental frequency spectrograms as well as the frequent observation of echoes without detectable lower hybrid waves suggests that the pre-existing 3 m field aligned irregularities responsible for the coherent echoes are likely not the result of the LHDI or an inverse cascade. These irregularities and density gradients could be originating at lower altitudes from adjacent latitudes and longitudes and drifting vertically, zonally, or meridionally above Jicamarca. As mentioned earlier, one of the possibilities is that the echoes could be originating from post-midnight spread-*F*. Multiple studies indicate the prevalence of equatorial spread-*F* in the postmidnight sector during low solar flux.

In a study by Hysell and Burcham (2002), the authors describe two types of post-midnight irregularities detected by the JULIA coherent radar that have no obvious correlation with geomagnetic activity as in the case of high altitude echoes. One class involves irregularities observed in the *F*-peak just before sunrise (Farley et al., 1970; Macdougall et al., 1998), and the other class is composed of remnants of plumes that might have formed several hours earlier and consists of dead bubbles as per Aggson et al. (1992) and Hysell and Burcham (2002). The authors suggest that the irregularities could continue to be excited by the density gradients or inhomogeneities even after the primary instability, such as ESF has ceased. These observations along with the more recent experiment by Hysell et al. (2020) lend credence to the idea that high altitude echoes may be originating from remnants of ESF produced at earlier local times and ascending in altitude.

All the echoes observed so far and listed in Table 1 are limited in altitude to ≈2,000 km. The lack of coherent echoes at higher altitudes could be due to the fact that depletion plumes associated with ESF cannot rise beyond a certain terminal altitude (Krall et al., 2010). Huba et al. (2008) ran SAMI3/ESF simulations in which they demonstrate that equatorial plasma bubbles can rise to altitudes up to 1,600 km for the parameters used in the simulation and stop rising or become fossil bubbles when the flux tube integrated ion mass density inside the bubbles is equal to that of the surrounding background. These fossilized bubbles have been observed in previous studies to occur later in the evening and can last until dawn (Makela et al., 2004). Additional simulations including light ions and with parameters representative of deep solar minimum conditions should be performed to further explore the terminal altitude.

Another possible reason for the high-altitude cutoff is the scattering geometry and the variation of the locus of perpendicularity with altitude. Future experiments with different antenna pointing positions could be performed to test this possibility.

In general, small scale differences in amplitude between the experimental LH sidebands in Figure 2 are reproduced in the simulation (shown in Figure 4). The difference in the simulation is within two orders of magnitude and agrees with the experiment (fourth panel of Figure 2). Therefore, it is possible that the difference in the sidebands seen experimentally could be accounted for by the inverse energy cascade mechanism.

## 6. Summary and Conclusion

We have demonstrated a mechanism that can explain the existence of lower hybrid spectral sidebands seen in high altitude postmidnight echoes above Jicamarca. This mechanism involves a lower hybrid drift instability (LHDI) paired with an inverse energy cascade. The role of weaker magnetic field intensities and lower densities present at higher altitudes and lower solar flux were shown to favor the inverse cascade mechanism, giving rise to discernible LH lines at 3 m wavelengths.

In contrast, the higher magnetic field intensities and densities associated with lower altitudes inhibit the cascade process and lead to weak or undetectable lower hybrid lines in the echoes. This result agrees with experimental data which indicates the prevalence of strong LH emissions at high altitudes.

Temporal fluctuations in the experimental LH lines suggest fluctuations in the waves produced by the LHDI which could be the result of the distribution and drifts of the density gradients in the echoes along with anomalous diffusion. However, the lack of fluctuations in the zero bin of the experimental spectrograms suggests that the coherent scatter is not produced by the same mechanism as lower hybrid waves, and is most likely due to pre-existing irregularities that formed elsewhere. These irregularities could then have ascended and drifted from lower altitudes, and adjacent latitudes and longitudes possibly from post-midnight ESF.

## Data Availability Statement

Data used for this publication are available through the CKAN open source data management system of the Jicamarca Radio Observatory (see https://www.igp.gob.pe/observatorios/radio-observatorio-jicamarca/database/project/jicamarca?data_type=Intermediate+Data).

**Acknowledgments**
The Jicamarca Radio Observatory is a facility of the Instituto Geofisíco del Perú operated with support from NSF award AGS-2213849 through Cornell. The help of the staff is much appreciated. We would like to acknowledge Dr. Joe Huba for helpful discussions related to the lower hybrid drift instability.

## References

Aggson, T. L., Maynard, N. C., Hanson, W. B., & Saba, J. L. (1992). Electric field observations of equatorial bubbles. *Journal of Geophysical Research*, *97*(A3), 2997–3009. https://doi.org/10.1029/90ja02356

Alken, P., Thébault, E., Beggan, C. D., Amit, H., Aubert, J., Baerenzung, J., et al. (2021). International Geomagnetic Reference Field: The thirteenth generation. *Earth Planets Space*, *73*, 49. https://doi.org/10.1186/s40623-020-01288-x

Bale, S. D., Mozer, F. S., & Phan, T. (2002). Observation of lower hybrid drift instability in the diffusion region at a reconnecting magnetopause. *Geophysical Research Letters*, *29*(24), 33-1–33-4. https://doi.org/10.1029/2002GL016113

Baumjohann, W., & Treumann, R. A. (1996). *Basic space plasma physics*. Imperial College Press. https://doi.org/10.1142/p015

Berthelier, J. J., Malingre, M., Pfaff, R., Seran, E., Pottelette, R., Jasperse, J., et al. (2008). Lightning-induced plasma turbulence and ion heating in equatorial ionospheric depletions. *Nature Geoscience*, *1*(2), 101–105. https://doi.org/10.1038/ngeo109

Burns, K. J., Vasil, G. M., Oishi, J. S., Lecoanet, D., & Brown, B. P. (2020). Dedalus: A flexible framework for numerical simulations with spectral methods. *Physical Review Research*, *2*(2), 023068. https://doi.org/10.1103/physrevresearch.2.023068

Derghazarian, S., Hysell, D. L., Kuyeng, K., & Milla, M. A. (2021). High altitude echoes from the equatorial topside ionosphere during solar minimum. *Journal of Geophysical Research: Space Physics*, *126*(2), e2020JA028424. https://doi.org/10.1029/2020JA028424

Farley, D. T., Balsley, B. B., Woodman, R. F., & McClure, J. P. (1970). Equatorial spread F: Implications of VHF radar observations. *Journal of Geophysical Research*, *75*(34), 7199–7216. https://doi.org/10.1029/ja075i034p07199

Hasegawa, A. (1975). *Plasma instabilities and nonlinear effects*. Springer-Verlag New York, Inc.

Huba, J. D. (1981). Diffusion of small-scale density irregularities during equatorial spread *F*. *Journal of Geophysical Research*, *7*(7), 9107–9114. https://doi.org/10.1029/ja086ia11p09107

Huba, J. D., Gladd, N., & Papadopoulos, K. (1978). Lower-hybrid-drift wave turbulence in the distant magnetotail. *Journal of Geophysical Research*, *83*(A11), 5217–5226. https://doi.org/10.1029/ja083ia11p05217

Huba, J. D., Hassam, A. B., & Winske, D. (1990). Stability of sub-Alfvénic plasma expansions. *Physics of Fluids B*, *2*(7), 1676–1697. https://doi.org/10.1063/1.859441

Huba, J. D., Joyce, G., & Feder, J. A. (2000). Sami2 is Another Model of the Ionosphere (SAMI2): A new low latitude ionosphere model. *Journal of Atmospheric and Terrestrial Physics*, *105*(A10), 23035–23053. https://doi.org/10.1029/2000ja000035

Huba, J. D., Joyce, G., & Krall, J. (2008). Three-dimensional equatorial spread *F* modeling. *Geophysical Research Letters*, *35*(10), L10102. https://doi.org/10.1029/2008GL033509

Huba, J. D., & Ossakow, S. L. (1981a). On 11-cm irregularities during equatorial spread *F*. *Journal of Geophysical Research*, *86*(A2), 829–832. https://doi.org/10.1029/ja086ia02p00829

Huba, J. D., & Ossakow, S. L. (1981b). Physical mechanism of the lower-hybrid-drift instability in a collisional plasma. *Journal of Atmospheric and Terrestrial Physics*, *43*(8), 775–778. https://doi.org/10.1016/0021-9169(81)90053-2

Huba, J. D., & Ossakow, S. L. (2000). An overview and synthesis of plasma irregularities in equatorial spread *F*. *Journal of Atmospheric and Solar-Terrestrial Physics*, *62*(12), 1037–1056. https://doi.org/10.1016/s1364-6826(00)00095-x

Hysell, D. L., & Burcham, J. D. (2002). Long term studies of equatorial spread *F* using the JULIA radar at Jicamarca. *Journal of Atmospheric and Solar-Terrestrial Physics*, *64*(12–14), 1531–1543. https://doi.org/10.1016/S1364-6826(02)00091-3

Hysell, D. L., Rao, S., Groves, K. M., & Larsen, M. F. (2020). Radar investigation of postsunset equatorial ionospheric instability over Kwajalein during project WINDY. *Journal of Geophysical Research: Space Physics*, *125*(6), e2020JA027997. https://doi.org/10.1029/2020ja027997

Hysell, D. L., Vierinen, J., Sultzer, M. P., Milla, M. A., & Obenberger, K. (2019). The case for combining a large low-band very high frequency transmitter with multiple receiving arrays for geospace research: A geospace radar. *Radio Science*, *54*(7), 533–551. https://doi.org/10.1029/2018rs006688

Kelley, M. C., & McClure, J. P. (1981). Equatorial spread-*F*: A review of recent experimental results. *Journal of Atmospheric and Terrestrial Physics*, *43*(5–6), 427–435. https://doi.org/10.1016/0021-9169(81)90106-9

Kelley, M. C., Pfaff, R., Baker, K. D., Ulwick, J. C., Livingston, R., Rino, C., & Tsunoda, R. (1982). Simultaneous rocket probe and radar measurements of equatorial spread *F* – Transitional and short wavelength results. *Journal of Geophysical Research*, *87*(A3), 1575–1588. https://doi.org/10.1029/JA087iA03p01575

Kraichnan, R. H. (1967). Inertial ranges in two-dimensional turbulence. *Physics of Fluids*, *10*(7), 1417–1423. https://doi.org/10.1063/1.1762301

Krall, J., Huba, J. D., Ossakow, S. L., & Joyce, G. (2010). Why do equatorial ionospheric bubbles stop rising? *Geophysical Research Letters*, *37*(9), L09105. https://doi.org/10.1029/2010gl043128

Lehtinen, M. S., & Häggström, I. (1987). A new modulation principle for incoherent scatter measurements. *Radio Science*, *22*(4), 625–634. https://doi.org/10.1029/RS022i004p00625

Liu, X., Chen, L., & Ma, Q. (2021). A statistical study of lower hybrid waves in the Earth's magnetosphere by Van Allen Probes. *Geophysical Research Letters*, *48*(10), e93168. https://doi.org/10.1029/2021gl093168

Macdougall, J. W., Abdu, M. A., Jayachandran, P. T., Cecile, J. F., & Batista, I. S. (1998). Presunrise spread *F* at Fortaleza. *Journal of Geophysical Research*, *103*(A10), 23415–23425. https://doi.org/10.1029/98ja01949

Makela, J. J., Ledvina, B. M., Kelley, M. C., & Kintner, P. M. (2004). Analysis of the seasonal variations of equatorial plasma bubble occurrence observed from Haleakala, Hawaii. *Annales Geophysicae*, *22*(9), 3109–3121. https://doi.org/10.5194/angeo-22-3109-2004

Mishin, E. V. (2013). Interaction of substorm injections with the subauroral geospace: 1. Multispacecraft observations of SAID. *Journal of Geophysical Research: Space Physics*, *118*(9), 5782–5796. https://doi.org/10.1002/jgra.50548

Norgren, C., Vaivads, A., Khotyaintsev, Y. V., & André, M. (2012). Lower hybrid drift waves: Space observations. *Physical Review Letters*, *109*(5), 055001. https://doi.org/10.1103/PhysRevLett.109.055001

Schunk, R. W., & Nagy, A. F. (2008). *Ionospheres physics, plasma physics, and chemistry* (2nd ed.). Cambridge University Press.

Seyler, C. E. (1991). Reduced magnetofluid dynamics in the lower-hybrid frequency range. *Physics of Fluids B: Plasma Physics*, *3*(9), 2449–2451. https://doi.org/10.1063/1.859616

Seyler, C. E. (1994). Lower hybrid wave phenomena associated with density depletions. *Journal of Geophysical Research*, *99*(A10), 19513–19525. https://doi.org/10.1029/94ja01572

Sulzer, M. P. (1993). A new type of alternating code for incoherent scatter measurements. *Radio Science*, *28*(6), 995–1001. https://doi.org/10.1029/93RS01918

Tsunoda, R. T. (1980). Backscatter measurements of 11-cm equatorial spread-*f* irregularities. *Geophysical Research Letters*, *7*(10), 848–850. https://doi.org/10.1029/gl007i010p00848

Vaivads, A., André, M., Buchert, S. C., Wahlund, J. E., & Fazakerley, A. N. (2004). Cluster observations of lower hybrid turbulence within thin layers at the magnetopause. *Geophysical Research Letters*, *31*(3), L03803. https://doi.org/10.1029/2003GL018142

Varney, R. H., Swartz, W. E., Hysell, D. L., & Huba, J. D. (2012). SAMI2-PE: A model of the ionosphere including multistream interhemispheric photoelectron transport. *Journal of Geophysical Research*, *117*(A6), 4–16. https://doi.org/10.1029/2011ja017280